

Numerical Investigation on Location of Protrusions and Dimples during Slot Jet Impingement on a Concave Surface using Hybrid ANN-GA

Alankrita Singh*

* Department of Mechanical Engineering, Indian Institute of Technology Madras, Chennai;
alankrita_92@rediffmail.com

Abstract: Numerical simulations using ANSYS Fluent 17.2 are explored for detailed discussion on jet impingement over a combined dimple and protrusion concave surface. Previous researchers have proved that both dimples and protrusions help in heat transfer augmentation. However combined effect of dimple and protrusion over a concave surface is still not studied. Therefore the present study is devoted to alternate location of dimple and protrusion over a concave surface for enhancement in impingement heat transfer. Simulations are performed for several arrangements of dimples and protrusions over a concave surface. It is noticed that particular arrangement of dimples and protrusions lead to increase in heat transfer compared to fully protruded or fully dimple concave surface. Further, it was also noticed that protrusions/ dimples at stagnation region degrade overall impingement heat transfer. At last the optimal location of dimples and protrusions is predicted using Artificial Neural network and specially formulated discrete version of GA.

Keywords: impingement cooling; concave surface; numerical simulation; dimple; protrusion; ANN; GA

1. Introduction

The Turbine Inlet Temperatures (TIT) is considerable increased in the past decade for higher efficiency of a gas turbine. In order to ensure desirable surface temperature of turbine blade, cooling of the vanes/blades are adopted. Jet impingement cooling is one of the effective methods incorporated at leading edge of a gas turbine blade for its cooling. For the purpose of describing the geometric specification of the leading edge; the circular profile is considered as the best model. Another application of impingement cooling involves annealing of metal, electronics cooling, de-icing of aircraft, power beaming etc. Pertinent papers on jet impingement deal mostly with flat surfaces and smooth concave surfaces.

Yadav et al. [1] experimentally proved that inclusion of protrusions increases heat transfer by 2.4-2.8 times in a rectangular duct. Chang et al. [2] investigated impingement heat transfer over a concave-dimpled surface. They obtained oval-shaped Nusselt number contours on the dimpled surface due to bursting phenomena associated with vertical flow structures. Dobberteau and Rahman [3] found spikes in Nusselt number where the jet interacts with abrupt change in geometry. Numerical study of heat transfer in a grooved micro-channel was performed by Kumar [4]. He claimed 16% increase in heat transfer performance by semi-circular grooves over rectangular grooves. This was attributed to modification in thermal boundary layer.

Lo and Liu [5] suggested incorporation of uniformly scattered roughness structures like pin fins, ribs or dimples for improvement in heat transfer. Liu et al. [6] said apart from grooved configuration the exit flow direction and the curvature of target plate also contributed in heat transfer variation. Du et al. [7] noticed varying heat transfer coefficient with the change in depth of dimples during their heat transfer investigation in a pin finned duct with dimples. Ligrani and Oliveria [8] stated that the flow characteristics created by the obstacles (protrusions, pin fins, rib turbulators, dimples) affects amount of impingement heat transfer.

During the assessment of turbulence Kannan and Sundararaj [9] found SST $k-\omega$ as better predicting tool for impingement heat transfer. This is in accordance with results of Kumar and Prasad [10].

Rib-dimple compound cooling in a channel was investigated by Choi et al. [11]. They noticed augmentation in heat transfer by compound channel compared to ribs/dimples alone. Similar observation was made by Singh and Ekkad [12] by using V-shaped ribs and dimples in a compound channel. Table 1 gives summary of heat transfer investigation on flat and concave surfaces with inclusion of dimples/ protrusions.

Table 1: Summary of augmentation in Nusselt number by various authors

Ref	Target geometry	Roughness element	Nusselt no. augmentation
[13]	flat	ribs	12.5-20%
[14]	concave	ribs	47.3%
[15]	rectangular channel	dimples	-60-0%
[16]	flat	dimples	6.2-26.4%
[17]	flat	protrusion	0.2-13%
[18]	concave channel	dimple/protrusion	21-30%
present study	concave surface	full dimple, full protrusion, combined dimple and protrusion	refer to results and discussion section 3

Because of symmetry in slot jet impingement, the problem is often modeled in two dimensional space (Fig. 1). Many results are available with two-dimensional approach for slot jet cooling with/without ribs in archival literature [19-23]. Agarwal and Bower [19] used two-equation $k-\epsilon$ model to enforce jet configuration applicable to VTOL aircraft design. Excellent agreement was obtained with the experimental data for under surface airframe pressure, ground level pressure and center-line speed decay along the jet axis. Two-dimensional simulation for an inclined and normal slot jet impingement on a flat plate was conducted by Ramezanpour et al. [20]. The simulated data were 1-3% different from experimental results. Rady and Arquis [21] simulated multiple slot jets in two dimensional space because of symmetry in the problem. Sharif and Mothe [22] carried out experiments and two-dimensional simulations for slot jet impingement over flat and concave surfaces. Among various turbulence models the SST $k-\omega$ mode accurately predicted the Nusselt number distribution with experimental data. Two-dimensional numerical simulations were used by Kadam et al. [23] to understand the flow physics on and around the rib elements.

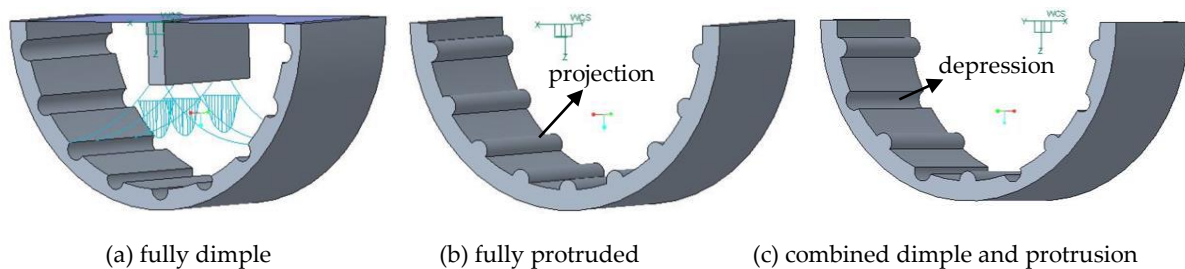


Figure 1. Various possible rough geometry over a concave surface. All the figures show axisymmetry in slot jet cooling

Foregoing discussion and from summary made in Table 1, it is evident that till now no investigation is made on compound rib/dimple over a concave surface which represents leading

edge of a gas turbine blade. Since heat transfer effects on flat and curved surfaces are different therefore the present work is focused on evaluation of different arrangements of combinations of dimples/protrusions over a concave surface (Fig. 1c) for effective slot jet impingement heat transfer.

2. Computational Model

As already discussed several investigations have proved that because of symmetry two dimensional studies for slot jet impingement problem is sufficient to determine corresponding heat transfer and flow characteristics. Therefore, two-dimensional steady state simulations using ANSYS Fluent 17.2 are carried out for the present study. Fig. 2 shows the computational model and its corresponding mesh. The maximum wall Y^+ value is always maintained around 1 by using fine mesh near the curved wall (Fig. 2b). A semi-circular concave plate ($D=160\text{mm}$, material-Aluminium) is used as the target surface. The target surface is uniformly heated at constant temperature of 335K which is cooled by perpendicular air jet coming out of a slot of width of 2mm . The protrusions and dimples are semi-circular concave surface with diameter of 3mm .

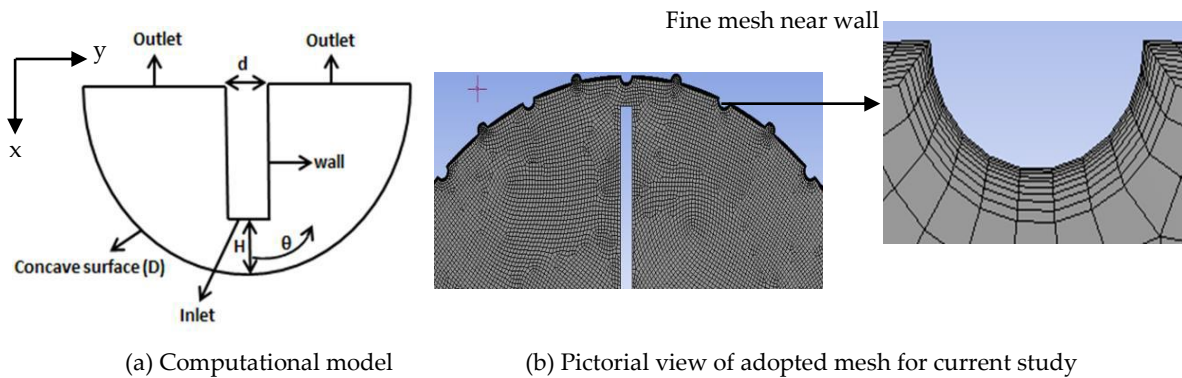


Figure 2. Computational model and pictorial view of typical mesh

Boundary conditions are implemented on the inlet of slot, outlet of concave surface (top and sides of concave plate) and on concave surface. The boundary conditions for this problem is as follow-

(i) Velocity inlet: For stream velocity and isothermal circumstances, a uniform velocity profile is used. ($u=u, v=0$) based on jet Reynolds number given by following equation-

$$Re = \frac{v\rho d}{\mu} \quad (1)$$

(ii) Pressure outlets: Pressure outlet boundary condition is employed on the top and sides of concave plate.

$$\frac{\partial u}{\partial x} = \frac{\partial v}{\partial x} = 0 \quad (2)$$

(iii) Walls: The walls of slot jet are at no slip condition and insulated.

$$q'' = 0 \quad (3)$$

$$u = v = 0 \quad (4)$$

(iv) Concave Plate: The target geometry is heated at constant temperature of 335K .

$$T_w = 335\text{K} \quad (5)$$

The flow air is considered to be incompressible with constant fluid properties. Buoyancy effects and viscous dissipations are neglected throughout the investigation. For all the simulations the turbulence intensity and turbulent viscosity are taken as 5% and 10 respectively. The flow is

assumed to be fully developed before the impingement. Reynolds averaged continuity, momentum and energy equations are used as governing equations as shown below-

Continuity equation:

$$\frac{\partial U}{\partial X} + \frac{\partial V}{\partial Y} = 0 \quad (6)$$

Momentum equation:

$$U \frac{\partial U}{\partial X} + V \frac{\partial U}{\partial Y} = \frac{\partial U}{\partial Y^2} - \frac{\partial P}{\partial x} \quad (7)$$

Energy equation:

$$U \frac{\partial U}{\partial X} + V \frac{\partial \alpha}{\partial Y} = \frac{1}{Pr} \frac{\partial^2 \alpha}{\partial Y^2} + Ec \left(\frac{\partial U}{\partial Y} \right)^2 \quad (8)$$

Where,

$$X = \frac{x}{d}, \quad Y = \frac{Re^{0.5} y}{d}, \quad V = Re^{0.5} \frac{y}{d}, \quad P = \frac{p - p_{\infty}}{\rho u_{\infty}^2} \quad (9)$$

$$\alpha = \frac{T - T_{\infty}}{T_w - T_{\infty}}, \quad Ec = \frac{u_{\infty}^2}{c_p} (T_w - T_{\infty}) \quad (10)$$

These equations are solved by pressure based solver using second order upwind scheme of discretization. Semi-Implicit Method for Pressure Linked Equation (SIMPLE) is incorporated for pressure velocity coupling. SST k- ω is used as the turbulence model. The solution is assumed to be converged when sum of the normalized residuals drop to 10^{-5} for momentum, continuity and turbulence equations and 10^{-7} for energy equations.

The jet Reynolds number is calculated according to equation (10).

$$Re = \frac{v \rho d}{\mu} \quad (11)$$

The Nusselt number and heat transfer coefficient are calculated creating custom field function in Fluent-17.2. The heat transfer coefficient is given by-

$$h = \frac{q''}{(T_w - T_{jet})} \quad (12)$$

Thereafter the Nusselt number formula is created using custom field function as-

$$Nu = \frac{hd}{k} \quad (13)$$

The streamwise local Nusselt number values are exported using CFD Post-17.2. Finally the local Nusselt number values are plotted along the length of plate (streamwise direction -x).

2.1 Validation and Grid Independent Study

Since no work is published on impingement cooling over a rough concave surface therefore, the validation of present study is made for smooth concave surface. This is achieved using average Nusselt number correlation provided by Sharif and Mothe [22]. The similar geometrical dimensions used in the study is used for its validation ($D=150\text{mm}$, $H/d=4$, $q''=5000\text{W/m}^2$). The validation is made with SST k- ω and Standard k- ϵ model. It is found from Fig. 3 that the calculation is more accurate with SST k- ω model (with maximum discrepancy of 5%) and hence acceptable.

Grid independent study is performed using grid convergence index method (GCI). Table 2 reports different size of meshes and y^+ chosen for performing grid independent study. For local Nusselt number variation along the streamwise direction of plate, 0.38% GCI value is obtained as shown in Fig. 4. Hence, simulations with grid size of 190000 nodes show grid independence for present numerical problem.

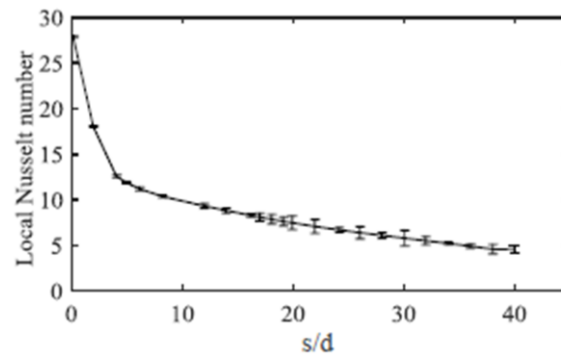


Figure 3. Validation of present study with correlation provided by Sharif and Mothe [22]

Table 2: Grid parameter for grid independence study

No. of nodes	y+	Average Nusselt number
155480	1.52	6.58
184622	1.14	7.31
190000	1.10	7.36

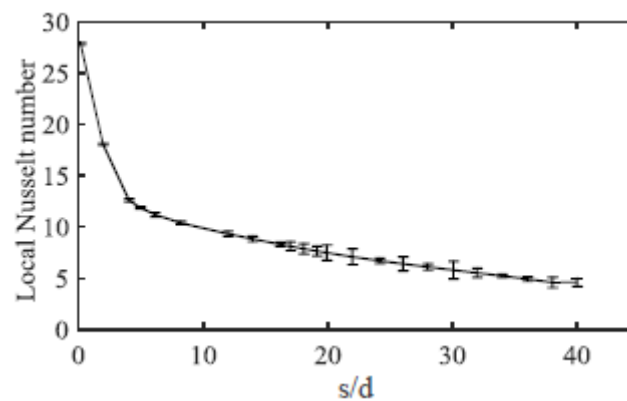


Figure 4. Local values of discretization error (GCI) of Nusselt number along the plate

3. Results and Discussion

Table 3 gives detail of location of dimple and protrusion considered during the present study. This includes concave surface with full dimples (cases- a_{d1} and a_{d2}), full protrusions (cases- a_{p1} and a_{p2}), alternate dimples and protrusions (cases- a_1, a_2, a_3, a_4, a_5 and a_6 and alternate dimples and protrusions except at stagnation point (case- a_7). For some of the cases the same simulation is repeated for different gap ratios and Reynolds number. The results of heat transfer are discussed in terms of dimensionless Nusselt number given by eq-13. Total 18 cases were simulated for the present study.

Table 3. Computational Matrix

Case no.	Location of dimple (°)	Location of protrusion (°)
a_{p1}	-	$\pm(0, 10, 20, 30, 40, 50, 60, 70, 80)$
a_{p2}	-	$\pm(0, 15, 30, 45, 60, 75)$
a_{d1}	$\pm(0, 10, 20, 30, 40, 50, 60, 70, 80)$	-
a_{d2}	$\pm(0, 15, 30, 45, 60, 75)$	-

a_1	$\pm(0, 20, 40, 60, 80)$	$\pm(10, 30, 50, 70)$
a_2	$\pm(10, 30, 50, 70)$	$\pm(0, 20, 40, 60, 80)$
a_3	$\pm(0, 30, 60)$	$\pm(15, 45, 75)$
a_4	$\pm(15, 45, 75)$	$\pm(0, 30, 60)$
a_5	$\pm(20, 60)$	$\pm(40, 80)$
a_6	$\pm(40, 80)$	$\pm(20, 60)$
a_7	$\pm(20, 60)$	$\pm(0, 40, 80)$

3.1. Effect of heat transfer with different geometries having same surface area

Fig. 5 shows local variation of Nusselt number for cases- a_{p1} , a_{d1} and a_2 . Although the available surface area for heat transfer is same for all the cases, the average and local Nusselt number values are different. This indicates change in fluid flow behaviour with the change in geometry of target surface. It can be inferred from the graph that all types of target surface show spikes in local Nusselt number where the jet meets abrupt change in geometry i.e., at the location where protrusions/dimples are placed. The spikes are formed due to change in thermal boundary layer because of inclusion of protrusions/dimples. The minimum Nusselt number is obtained at the edges of target surface because of flow separation and formation of counter rotating vortices at the ends of the surface.

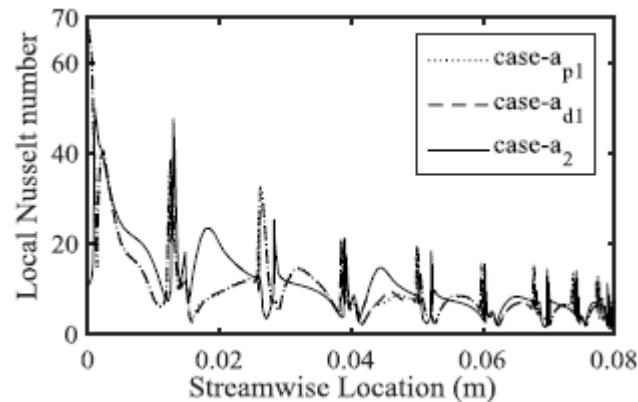


Figure 5. Local variation of Nusselt number

Fig. 6 shows velocity streamlines for cases- a_{p1} , a_{d1} and a_2 . All the streamlines show symmetrical distribution along the jet centreline and entrainment of air from the top. The enlarged view of streamlines shows recirculating vortices at one of the end of notches protrusions and inside the dimple cavity. The recirculation zones obstruct flow of cold air near the target surface and reduce heat transfer. The overall improvement in heat transfer occurs because of directing the flow towards the wall jet region as identified by reattachment of streamlines in Fig. 6. Similar observation was also made by previous investigators [13, 24-25].

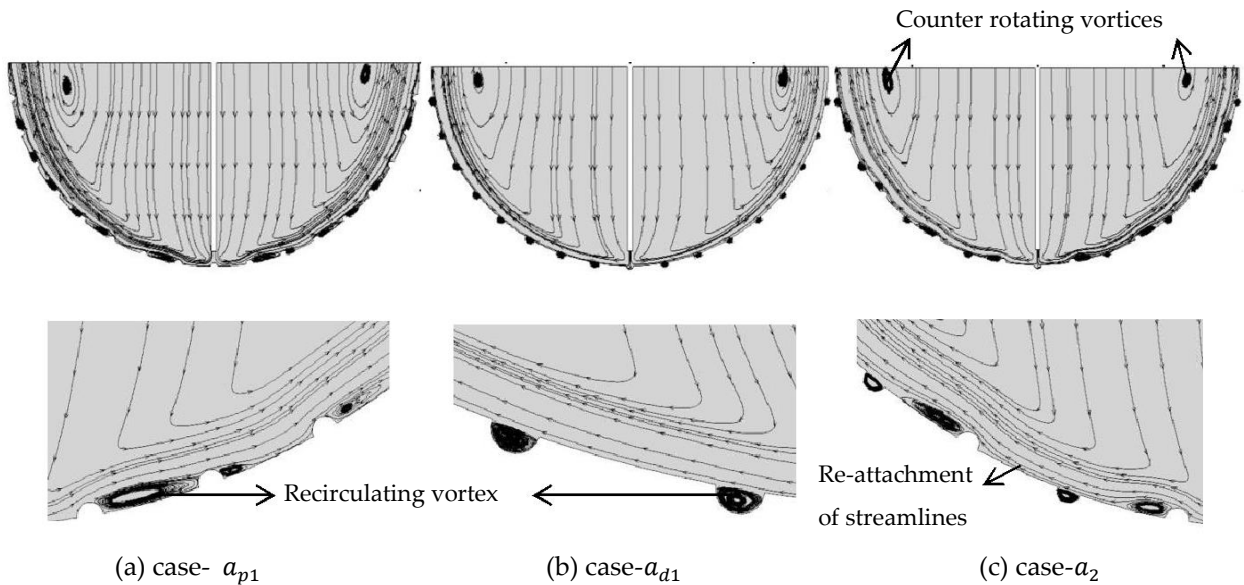


Figure 6. Velocity streamlines for air jet impingement over a concave surface with (a) full protrusions (b) full dimples (c) combined dimples and protrusions. The bottom figures show the enlarged view of streamlines near protrusion/dimple.

One of the important observations made is the combined protruded and dimpled target surface (case- a_2) performs better than fully dimpled (case- a_{d1}) or fully protruded case (case- a_{p1}). This outcome is important considering the fact that protrusions increase the weight of target geometry and dimples increase local stresses and reduce weight. Hence proper arrangement of dimples and protrusions is helpful for better heat transfer and life span of turbine blade. For all the cases the highest Nusselt number is attained at the stagnation point. This is obvious because the jet impacts the surface with its full intensity at the centre of the plate.

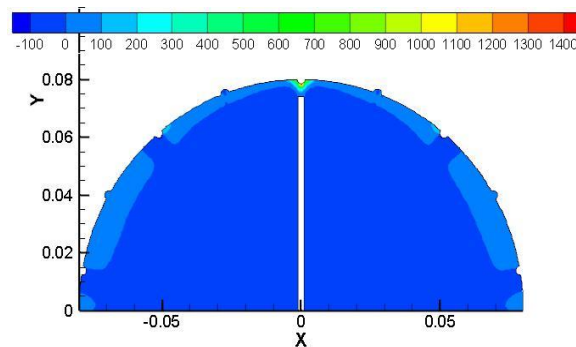


Figure 7. Pressure contour for case- a_2

It is also seen that notches of the protrusions always degrade heat transfer. This is because of the formation of negative pressure zone at the notches of protrusion facing the exit of target surface as shown in Fig. 7. The negative pressure leads to formation of recirculating vortex near the rough geometry as presented in Fig. 6. These recirculating vortices are responsible for degradation in heat transfer near the notches of protrusion which is shown by downward slopes in local Nusselt number plot of Fig. 5.

3.2. Effect of inclusion of protrusion/dimple except at stagnation point

Fig. 8 shows streamwise local Nusselt number variations between cases- a_6 and a_7 . It is noticed that inclusion of protrusions/dimples are not effective if they are placed at stagnation point

i.e., centre of the plate. As the jet hits the target surface it spreads equally on both sides and starts deteriorating its strength after covering certain distance along the circumference of the target surface. If protrusion/dimple is placed at the stagnation point, the stagnation Nusselt number decreases. This happens because of initiation of detachment of streamlines just from the centre of protrusion as shown in Fig. 6. Earlier detachment of streamlines leads to reduction of effective jet impingement region.

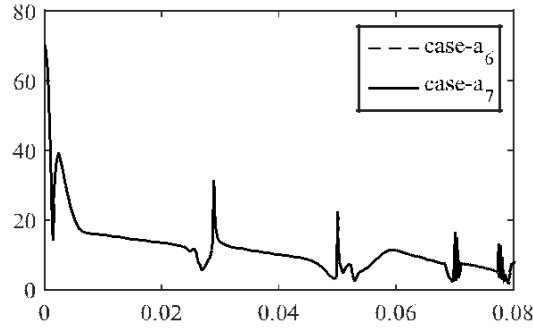


Figure 8. Local variation of Nusselt number

Another explanation to this phenomenon can be given from contours of turbulence kinetic energy. As seen from Fig. 9 the turbulence kinetic energy at the centre of the plate is higher for case-a₆ (no protrusion/dimple at centre) compared to case-a₇. The plot of local Nusselt number of Fig. 8 is consistent with contours of turbulent kinetic energy of Fig. 9.

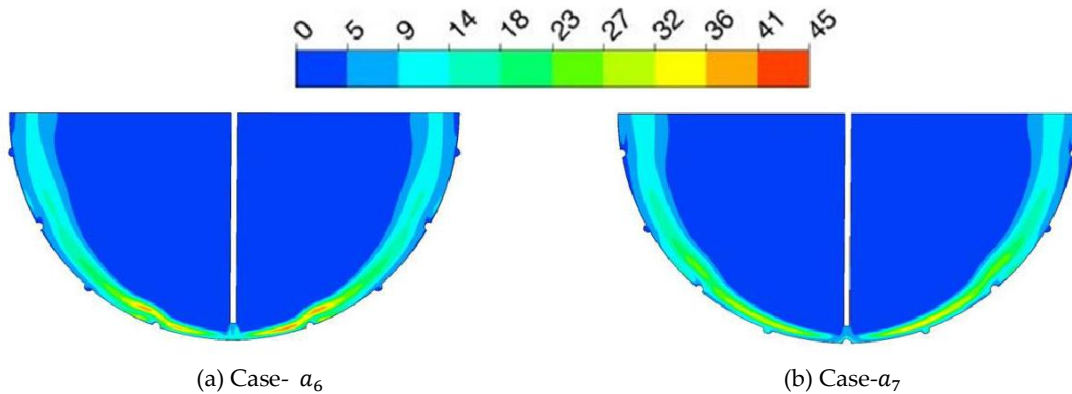


Figure 9. Contours of Turbulent Kinetic Energy

3.3. Effect of heat transfer on Reynolds number and gap ratio

Fig. 10 shows average Nusselt number variation with increasing Reynolds number for case-a₅. It is observed that the performance of heat transfer starts improving with the increase of Reynolds number. This happens because of increase in jet momentum and energy with the increase of Reynolds number. However the increment of Reynolds number is accompanied with increase in pressure drop as depicted from Table 4. For 62.5% of increment in Reynolds number there is 52% and 62% increase in average Nusselt number and pressure drop respectively. At higher Reynolds number (Re=8122) for 100% hike in Reynolds number there is 83.7% and 287% increase in average Nusselt number and pressure drop respectively. Sudden rise in pressure drop at higher Reynolds number is in accordance with pumping power being proportional to cube of flow velocity. This suggests there lays an optimum value of Reynolds number at which best heat transfer performance is obtained without appreciable amount of pressure loss.

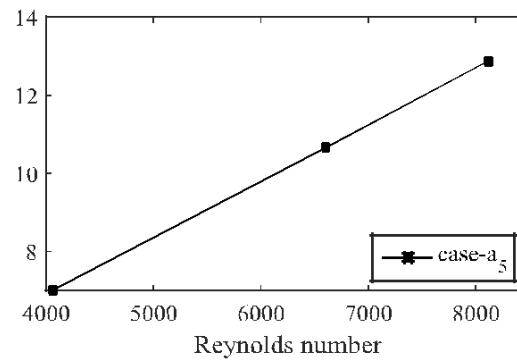


Figure 10. Reynolds number effect on average Nusselt number

Table 4. Average Nusselt number and pressure drop for various Reynolds number for case-a5

Reynolds number	Nu_{avg}	ΔP (Pa)
4061	7.02	11.47
6600	10.66	30.34
8121	11.90	44.46

Contrary to Reynolds number the performance of rough geometries on heat transfer degrades with the increment of gap ratio for combined dimpled and protruded concave surface as shown in Fig. 11. This happens due to increase in distance of target surface from potential core length where the jet loses its momentum to neighboring fluids and thus degrades convective heat transfer.

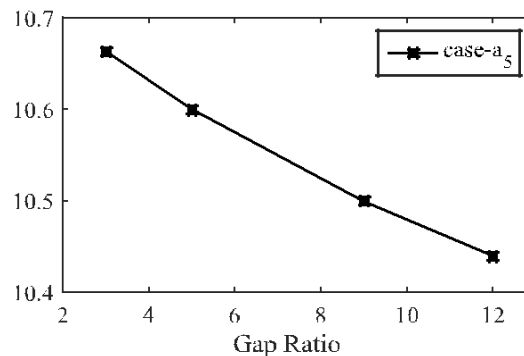
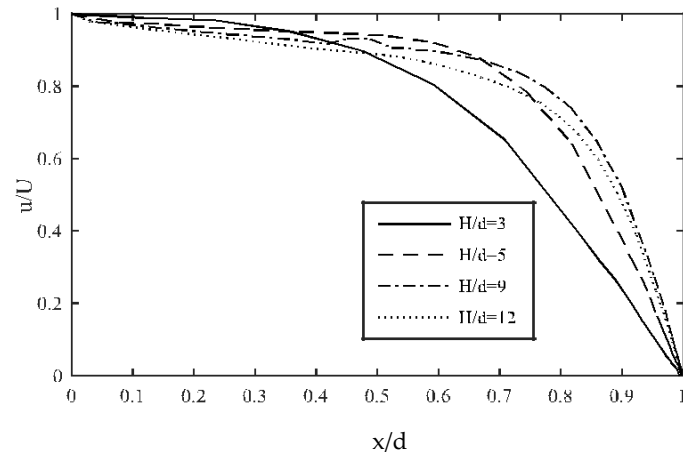


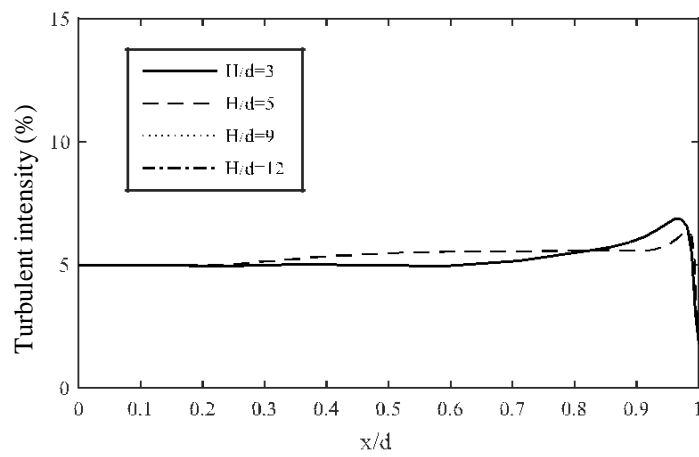
Figure 11. Reynolds number and gap ratio effect on average average Nusselt number for case-a5

If one looks at the velocity profile and turbulence intensity along the jet axis then the heat transfer results may seem to contradict the kinetic energy theorem. Fig. 12 shows that both the centre line jet velocity as well as turbulence intensity dominates for higher gap ratios compared to its lower values. This indicates that the heat transfer would be higher for higher gap ratios but the reverse happened as local Nusselt number profile along streamwise direction is presented in Fig. 13. Both the stagnation as well as average Nusselt number is higher for gap ratio of 3 than compared to any other higher values of gap ratios considered. The deviation for stagnation and average Nusselt number between gap ratios of 3 and 12 is 7.4% and 3.6% respectively.

Fig. 14 depicts clearly how the high turbulent kinetic energy of jet is getting lost while mixing with entrained air from atmosphere just before reaching the stagnation region. This loss in turbulence kinetic energy of jet while moving downstream results in lower average Nusselt number at higher gap ratios.



(a) Effect of gap ratio on velocity profile along jet axis



(b) Effect of gap ratio on turbulent intensity along jet axis

Figure 12. Effect of gap ratio on flow parameters for case- a_5

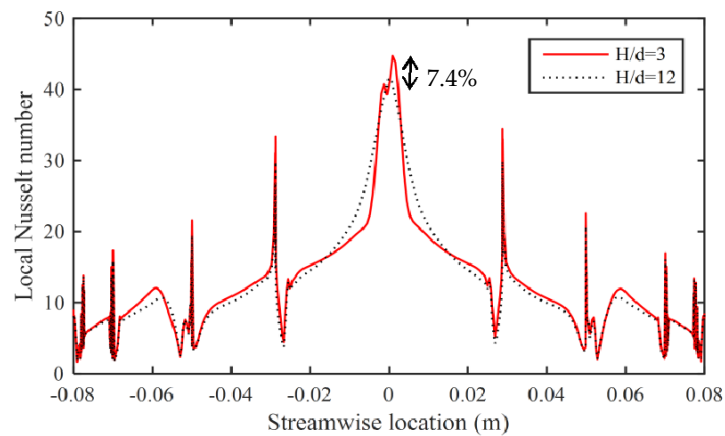


Figure 13. Effect of local Nusselt number along streamwise direction

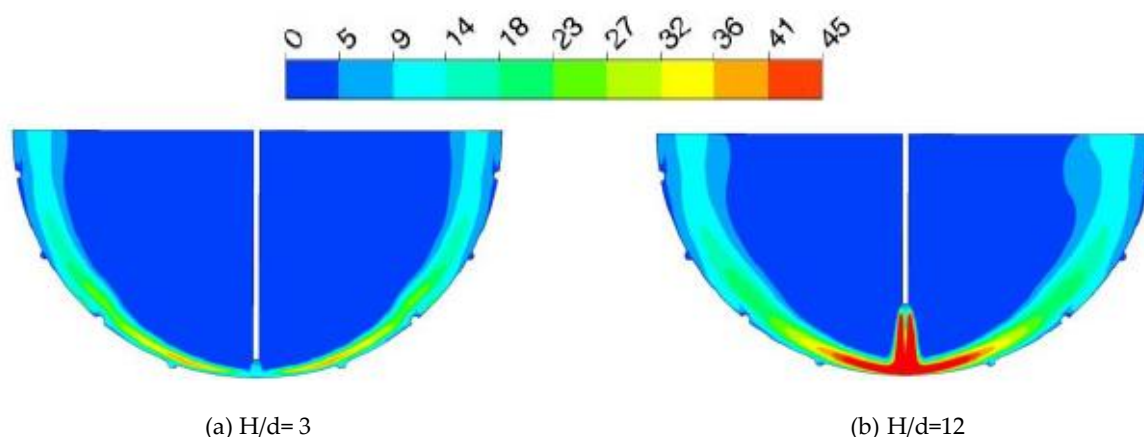


Figure 14. Variation of turbulence kinetic energy with gap ratio for case- a_5

4. Optimization

Artificial neural network (ANN), Genetic Algorithm (GA) and their coupling are recent techniques developed for mathematical modelling and optimization of heat transfer problems. GA works by encouraging the less suitable individuals in the population to die and selectively choosing the fittest individuals. GA finds solution (maximum or minimum value in the search space) as evolution proceeds. Haasenritter and Weigand [26] implemented GA to optimize ribs inside a turbine cooling channel. Yang and Chen [27] optimized geometrical dimension of two dimensional ribbed channel using GA. ANN is a mathematical model based on the architecture of biological neurons. It relates input and output by changing the link relationships between internal nodes. ANN is helpful in addressing complex non-linear relationship and predicting output based on the trend of previous data in a search space. Damavandi et al. [28] coupled ANN with GA to obtain optimum configuration of ribs for maximum heat transfer and minimum pressure drop in a ribbed channel. Similar method was also adopted by Xi et al. [29] for optimization of rib dimensions in a ribbed channel. Damavandi et al. [30] used CFD results for optimization of wavy fin heat exchangers using NSGA algorithm.

Previous section confirms that combined dimples and protrusions perform better at gap ratio of 3. If one tries to obtain the location of protrusions and dimples at which highest heat transfer is obtained then several hit and trial method is required. The total number of possible cases subject to alternate location of protrusion/dimple with minimum angular difference of 5° (i.e., $0^\circ, 5^\circ, 10^\circ, \dots, 75^\circ, 80^\circ, 85^\circ$) will be 2^{18} . Simulating these many cases would consume enormous time.

Therefore, this is accomplished with Artificial Neural Network (ANN) and developed code for discrete Genetic Algorithm (GA). The fitness function for discrete GA is created using ANN. The ultimate aim of ANN is to avoid time consuming numerical simulation.

4.1. Structure of ANN Model

For better statistical significance with ANN, it is necessary to have a sufficient amount of training data to cover the full spectrum of the network and safe applicability. Total 175 cases with different locations of dimples and protrusions are randomly created and simulated to use for feed forward ANN model. For ease of ANN modelling the locations of dimples and protrusions are converted into binary bits (0,-1,1) where '0' indicates absence of any protrusions/dimples and '-1' and '1' represents existence of dimples and protrusions respectively. Table 5 presents few configurations of combined dimples and protrusions with their binary bits.

The building of ANN model begins with 18 nodes (18 possible locations for dimples and protrusions) in input layer and one node in output layer (corresponding average Nusselt number of any configuration). There was no change in the output value with the change in the number of hidden layers. Hence single hidden layer is chosen for present neural network. Neuron

independence study is carried out to determine the number of nodes in the hidden layer. This is accomplished by several trial and error methods which give lower mean square error (MSE) and higher correlation coefficient (R) which are determined as follow-

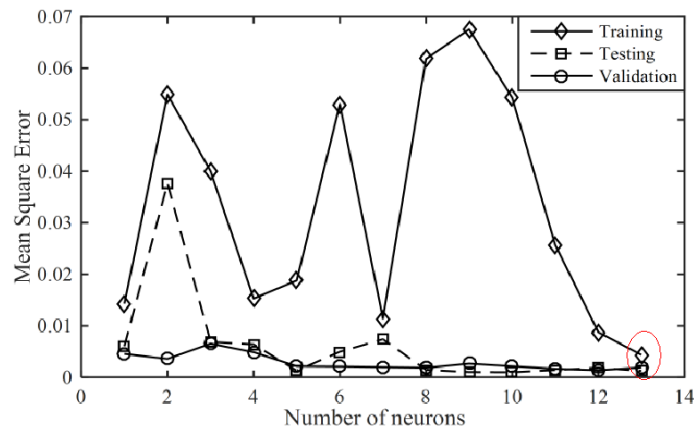
$$MSE = \frac{1}{N} \sum_{i=1}^N (\phi_{ANN,i} - \phi_{data,i})^2 \quad (14)$$

$$R = \frac{C_v(data, ANN)}{\sqrt{C_v(data, data)} \sqrt{C_v(ANN, ANN)}} \quad (15)$$

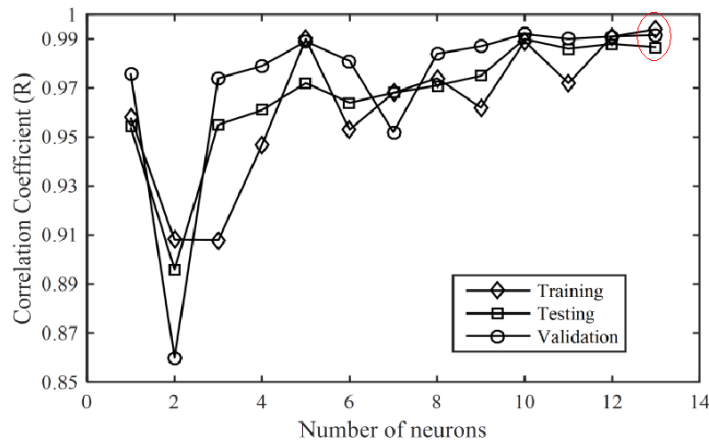
Where, ϕ_{ANN} is predicted value from ANN, ϕ_{data} is output value from simulation, C_v is covariance. The Levenberg-Marquardt training algorithm is used. The exercise for neuron independence study is shown in Fig. 15.

Table 5. Binary bits for combined dimple protruded concave surface

Location of protrusions	Location of dimples	Binary bits for 'θ' corresponding to 5°,10°,15°,20°,25°,30°,35°,40°,45°,50°,55° ,60°,65°,70°,75°,80°,85°
±(0°, 20°, 40°,60°,80°)	±(10°,30°,50°,70°)	1,0,-1,0,1,0,-1,0,1,0,-1,0,1
±(25°,65°)	±(5°,45°,85°)	0,-1,0,0,1,0,0,0,-1,0,0,0,1
±(10°,40°,70°)	±(25°,55°,85°)	0,0,1,0,0,-1,0,0,1,0,0,-1,0,0,-1



(a) MSE at different number of neurons



(b) Correlation coefficient at different number of neurons

Figure 15. Neuron independence test

Fig. 16 represents the typical structure of ANN model used in this study. The selected model has 18-13-1 structure which means 18 nodes in the input layer, 13 nodes in the hidden layer and 1 node in the output layer.

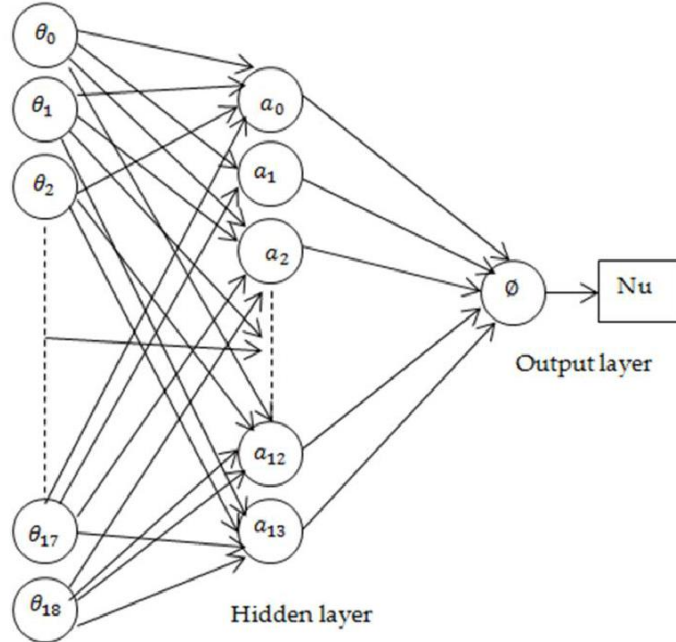


Figure 16. Architecture of ANN model used in the present study

In Fig. 16 the bias unit and is for the input and hidden layer respectively which is taken as 1. Sigmoid transfer function and linear function is used as the neuron function for hidden layer and output layer respectively. These functions are given by following equations-

$$f(n) = \frac{2}{1 + e^{-2n}} - 1 \quad (16)$$

$$g(n) = pn \quad (17)$$

Where, 'n' is input value and 'p' is a constant whose value is determined during ANN fitting. By default all the input data to ANN is decoded between -1 and 1 whose formulation is given by eq-18.

$$\phi = \frac{\phi_{max} - \phi_{min}}{\theta_{max} - \theta_{min}} (\theta - \theta_{min}) + \phi_{min} \quad (18)$$

Where, ' θ ' is any input variable and ' ϕ ' is the corresponding encoded value for the input variable whose range is between -1 to 1. The gain in input variable (G_1) is defined as follow-

$$G_1 = \frac{\phi_{max} - \phi_{min}}{\theta_{max} - \theta_{min}} \quad (19)$$

Now, the neuron vector is given by

$$a_{13 \times 1} = f(w_{13 \times 19}^{(1)} \cdot \theta_{18 \times 1}) \quad (20)$$

Here, ' $w^{(1)}$ ' is the weight matrix and ' θ ' is matrix of input variables with encoded values between the range of -1 to 1 according to eq-18.

The encoded neuron unit for the output layer is calculated as-

$$\phi = w_{1 \times 14}^{(2)} \cdot \begin{bmatrix} a_0 \\ [a_i]_{18 \times 1} \end{bmatrix} \quad (21)$$

Here, ' $w^{(2)}$ ' is the weight matrix for hidden layer. Comparing eq-17 and eq-21 gives-

$$p = w_{1 \times 14}^{(2)} \text{ and } n = a \quad (22)$$

Finally, ' ϕ ' is reversed mapped to get final value of average Nusselt number according to eq-23.

$$Nu = (\phi - \phi_{min}) \left(\frac{1}{G_2} \right) + Nu_{min} \quad (23)$$

4.2. Selection of training data and accuracy of ANN

Before training simulated data to ANN, 15% of the data sets are left aside for validation of developed neural network model. The remaining 85% of simulated data sets is assigned for input to ANN. Among 80%, 10% and 10% of total input data are assigned for training, testing and validation respectively. Fig. 17 shows the corresponding regression plots. The R-values for training, validation and test data sets are 0.994, 0.986 and 0.991 respectively. R-values closer to unity indicate strong relationship between targets and output.

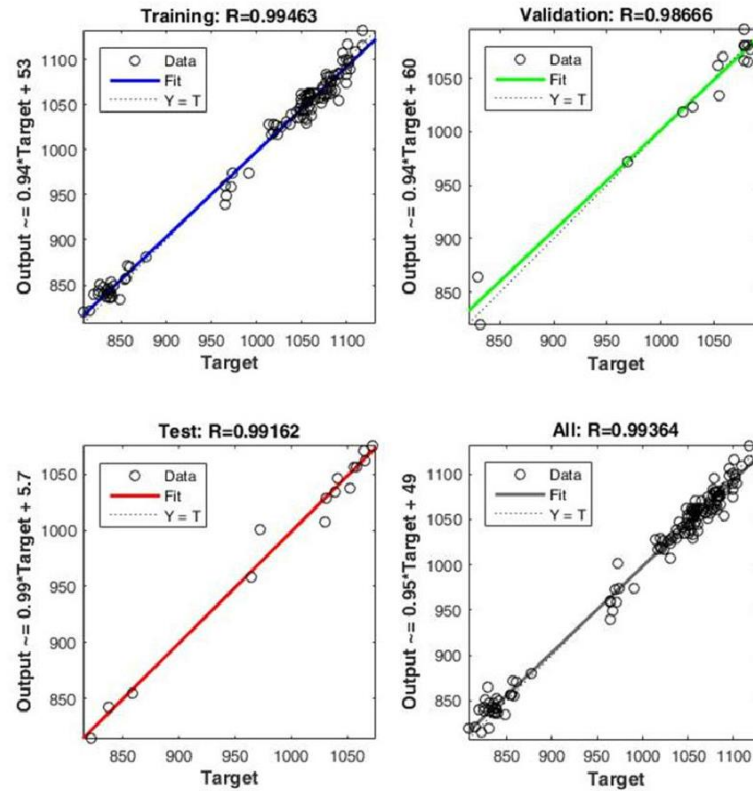


Figure 17. Regression analysis of proposed ANN model in training, validation and testing data sets

The optimal weights of proposed ANN model are:

$$w_{13 \times 19}^{(1)} = \begin{bmatrix} 1.58 & -0.14 & -0.05 & -0.2 & 0.31 & -0.61 & 0.29 & -0.21 & 0.43 & 0.687 & 0.442 & -0.02 & 0.45 & -0.5 & -0.61 & 0.11 & -0.2 & 0.41 & -0.57 \\ -1.35 & 0.46 & -0.16 & 0.164 & 0.11 & -0.54 & -0.2 & 0.136 & -0.58 & -0.41 & -0.01 & -0.19 & -0.5 & 0.73 & -0.01 & 0.27 & 0.77 & 0.01 & -0.13 \\ 1.07 & -0.25 & -0.22 & 0.274 & 0.02 & -0.43 & -0.1 & -0.02 & -0.07 & -0.7 & -0.67 & 0.45 & 0.51 & 0.42 & -0.58 & -0.2 & 0.2 & -0.2 & 0.39 \\ -0.8 & 0.12 & -0.39 & -0.44 & -0.2 & -0.04 & -0.6 & -0.28 & -0.11 & -0.3 & -0.64 & -0.33 & 0.58 & -0.6 & 0.15 & -0.1 & -0.1 & 0.21 & 0.54 \\ 0.54 & 0.02 & 0.29 & -0.01 & 0.48 & -0.02 & -0.5 & 0.163 & -0.07 & -0.08 & 0.318 & 0.567 & -0.6 & 0.64 & 0.17 & 0.51 & 0.09 & 0.44 & -0.56 \\ -0.33 & 0.56 & 0.25 & 0.047 & 0.22 & 0.534 & -0.1 & -0.63 & 0.118 & -0.84 & -0.17 & -0.13 & 0.45 & -0.6 & -0.06 & -0.1 & 0.28 & 0.01 & 0.17 \\ -0.04 & 0.33 & 0.33 & 0.283 & -0.11 & -0.24 & -0.7 & 0.464 & -0.2 & -0.39 & -0.48 & 0.42 & 0.21 & 0.04 & 0.48 & -0.2 & -0.4 & 0.53 & -0.36 \\ 0.24 & 0.39 & -0.52 & -0.46 & 0.4 & 0.254 & 0.51 & -0.6 & 0.324 & -0.27 & -0.02 & 0.128 & 0.23 & 0.35 & 0.24 & -0.2 & -0.4 & 0.45 & -0.44 \\ 0.56 & 0.47 & -0.57 & -0.46 & 0.17 & 0.305 & 0.42 & 0.25 & -0.03 & -0.18 & -0.47 & -0.34 & -0.4 & -0.3 & -0.51 & -0.3 & -0 & -0.5 & -0.38 \\ -0.88 & -0.11 & 0.56 & -0.25 & -0.59 & -0.4 & 0.58 & 0.06 & -0.73 & -0.33 & 0.126 & -0.22 & -0.5 & 0.39 & 0.26 & 0.18 & -0.1 & -0.1 & -0.21 \\ -1.07 & -0.16 & 0.06 & 0.106 & -0.11 & -0.05 & -0.1 & 0.072 & 0.738 & -0.47 & -0.09 & -0.32 & 0.56 & -0.6 & 0.65 & -0.4 & -0.4 & -0.5 & 0.06 \\ 1.39 & 0.2 & 0.26 & -0.55 & -0.3 & -0.08 & 0.46 & -0.58 & -0.54 & -0.04 & 0.093 & 0.544 & 0.23 & 0.3 & -0.44 & -0.6 & -0.3 & -0.1 & -0.22 \\ 1.68 & 0.45 & -0.12 & -0.35 & -0.45 & -0.22 & 0.23 & -0.51 & -0.41 & -0.43 & -0.12 & -0.51 & -0.4 & -0.1 & 0.19 & 0.43 & -0.2 & 0.66 & -0.46 \end{bmatrix} \quad (25)$$

$$w_{1 \times 14}^{(2)} = \begin{bmatrix} 0.17 & -0.91 & 0.15 & -0.04 & 0.36 & 0.59 & -0.6 & -0.26 & -0.2 & -0.7 & -0.8 & 0.46 & 0.44 & 0.87 \end{bmatrix} \quad (26)$$

Finally, the average Nusselt number is calculated according to eq-18, eq-20, eq-21 and eq-23. The validation of developed neural network model with 15% of previously kept aside data is shown by parity plot in Fig. 18. The result indicates the ability of ANN to accurately forecast the average Nusselt number with an uncertainty of $\pm 1\%$. The designed neural network simulation function is carried further for coupling with specially formulated discrete GA.

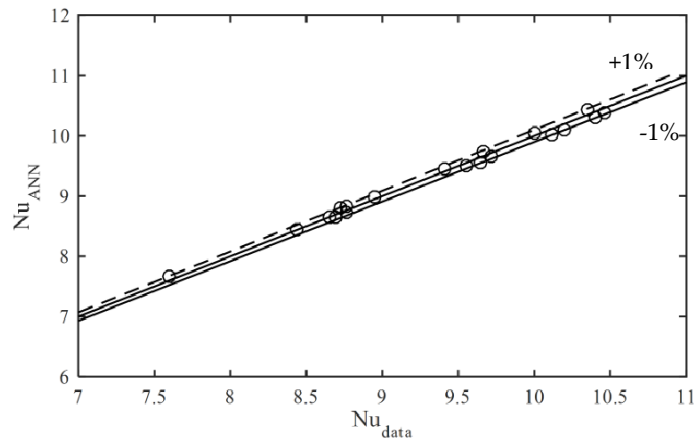


Figure 18. Parity plot for testing of predicted results by ANN with simulated data

4.3. Optimization in heat transfer using hybrid ANN-GA

While ANN is basically used for problems whose solutions do not follow a linear pattern, GA is used to select the survival of the fittest (best solution). The objective of present problem is to maximize average Nusselt number during slot jet impingement on a combined dimpled and protruded concave surface. Mathematically,

$$\text{Maximize } Nu = f(\theta_1, \theta_2, \dots, \theta_{17}, \theta_{18}) \quad (27)$$

$$\text{Subject to constraints: } 0^\circ \leq \theta \leq 85^\circ \quad (28)$$

where, θ can hold only discrete values of -1, 0 and 1 according to the formulation given in Table 6.

This is solved by integrating ANN with GA. The fitness function to GA is provided by ANN output. Since, the input to ANN was given in binary bits with the condition of alternate location of protrusions and dimples and the Matlab GA toolbox is suited only for unconstrained problem therefore, especially formulated discrete version of GA tool of MATLAB 2017b is used for the present problem of optimization. A separate function for constraints is also created and coupled to the formulated GA tool. The upper and lower bound constraints for 18 variables of the present problem are-

$$\begin{bmatrix} lb \\ ub \end{bmatrix} = \begin{bmatrix} -1 & -1 & -1 & -1 & -1 & -1 & -1 & -1 & -1 & -1 & -1 & -1 & -1 & -1 & -1 & -1 & -1 \\ 1 & 1 & 1 & 1 & 1 & 1 & 1 & 1 & 1 & 1 & 1 & 1 & 1 & 1 & 1 & 1 & 1 \end{bmatrix} \quad (29)$$

The formulated GA constitute of several functions for creation, mutation and crossover. The creation function creates an initial population satisfying bounds and integer constraints. Mutation function creates the mutated children using the Gaussian distribution. Crossover function decides how many offspring to produce and to allocate space to them. A separate discrete bound function is created to make all variables to fall inside the bounds.

Further a separate constraint function is also created to satisfy the following conditions-

(i) Alternate location of protrusions and dimples such that a protrusion is always followed by a dimple and vice versa



(ii) The distance between any alternate two dimples and protrusions for particular configuration is always constant.



The discrete bound function and constraint function is coupled to GA toolbox. The property of formulated GA algorithm is given in Table 6. The population size was varied from 50 to 200 with an interval of 50. There was no change in the output value with the increase in population size after 150. Hence, the population size is taken as 150.

Table 6. Property of GA algorithm

Parameter	Values
Population size	150
Generation limit	50
No. of generations	100
Crossover fraction	0.5
Mutation probability	0.7

The obtained optimized configuration from proposed hybrid ANN-GA gives $(10^\circ, 30^\circ, 50^\circ, 70^\circ)$ location for dimples and $(20^\circ, 40^\circ, 60^\circ, 80^\circ)$ for protrusions. The optimized configuration is simulated to check the accuracy of proposed hybrid ANN-GA model. The difference between both the data is only 1.2%. Hence, the solution given by ANN-GA model is optimal and acceptable.

4. Conclusions

Numerical investigation of slot jet impingement heat transfer is carried over a leading edge of a gas turbine blade modified with inclusion of dimples and protrusions over its inner wall. The major conclusions drawn from the present study are as follow-

(a) Combined dimple and protruded concave surface provides higher impingement heat transfer compared to fully protruded or fully dimpled surface.

(b) Same surface area of target surface can lead to different impingement heat transfer values depending on the location of dimples and protrusions over the target surface.

(c) The local Nusselt number profiles show spikes where the jet meets abrupt change in geometry because of change in thermal boundary layer.

(d) Notches of the protrusions are responsible for degrading overall effect of convective heat transfer because of formation of recirculation.

(e) Inclusion of dimple/protrusion at the stagnation point reduces region of effective impinging effect. Therefore, overall heat transfer performance is better if no dimples/protrusions are placed at the stagnation point.

(f) The performance of heat transfer ameliorates with the increase of Reynolds number but here exists an optimum range of Reynolds number while considering combined effect of pressure drop and heat transfer together.

(g) The average Nusselt number decreases with the increase in the value of gap ratio due to increase of distance between target surface and potential core length of jet and thereafter losing its energy to surrounding fluid before reaching the target surface.

(h) ANN is used as a surrogate model to explore heat transfer associated with various possible locations of dimples/protrusions.

(i) A specially formulated discrete version of GA is used to optimize location of protrusions and dimples for highest heat transfer.

Nomenclature

c_p	Coefficient of pressure (dimensionless)
d	diameter of jet (m)
D	Diameter of concave plate
h	Heat transfer coefficient (W/m ² -K)
H	Jet-to-plate distance (m)
k	Thermal conductivity of air (W/m-K)
Nu	average Nusselt number
p	pressure (Pa)
Pr	Prandtl number
q''	Heat flux (W/m ²)
Q	Amount of heat transferred (W)
SST	Shear Stress Transport
T	Temperature (K)
u, v	Component of velocity along x, y direction (m/sec)
x, y	coordinates along and normal to the plate
y^+	Non-dimensional distance (dimensionless)

Greek symbols

θ	Angle between centre of plate to centre of protrusion/dimple (°)
ρ	Density (kg/m ³)
μ	Dynamic viscosity (kg/m-sec)
∞	free stream value
Δ	difference

Subscripts

jet	jet
w	wall

Acknowledgments: The authors would like to acknowledge Ministry of Human Resource Development, Government of India for providing financial assistance during the research program. The author would also like to acknowledge Prof. B.V.S.S.S Prasad and Prof. C. Balaji for teaching the basic concepts. Mr. Abhishek Parmar and Mr. K.E. Sai Kumar are acknowledged for giving suggestions during formulation of discrete GA function.

Conflicts of Interest: The author declares no conflict of interest.

References

1. Yadav, S., Varun, Siddhartha, Kaushal, S. Heat Transfer and Frictional Characteristics of Rectangular Channel Air Heater Duct Having Protrusion as Roughness Elements. *Int. J. Engg. Series C*. **2012**, 93(4), 307-312.
2. Chang, S.W., Chiou, S.F., Chang, S.F. Heat transfer of impinging jet array over concave dimpled surface with applications to cooling of electronic chipsets. *Exp. Therm. Fluid Sci.* **2007**, 31(7), 625-640.
3. Dobbertean M.M. and Rahman, M.M. Numerical analysis of steady state heat transfer for jet impingement on patterned surfaces, *Appl. Therm. Engg.* **2016**, 103, 481-490.
4. Kumar, P. Numerical investigation of fluid flow and heat transfer in trapezoidal microchannel with groove structure. *Int. J. Therm. Sci.* **2019**, 136, 33-43.
5. Lo, Y-H. and Liu, Y-H. Heat transfer of impinging jet arrays onto half-smooth, half-rough target surfaces. *Appl. Therm. Engg.* **2018**, 128, 79-91.
6. Liu, Y.H., Song, S-J., Lo, Y-H. Jet impingement heat transfer on target surfaces with longitudinal and transverse grooves. *Int. J. Heat Mass Transf.* **2013**, 58, 292-299.
7. Du, W., Luo, L., Wang, S., Zhang, X. Flow Structure and Heat Transfer Characteristics in a 90-Deg Turned 573 Pin Fined Duct With Different Dimple/Protrusion Depths. *Appl. Therm. Engg.* **2019**, 146, 826-842.
8. Ligrani, P.M. and Oliveria, M.M. Comparison of heat transfer augmentation techniques. *AIAA J.* **2003**, 41, 575 337-362.
9. Kannan, B.T. and Sundararaj, S. Steady state jet impingement heat transfer from axisymmetric plates with 577 and without grooves. *Procedia Engg.* **2015**, 127, 25-32.
10. Kumar, B.V.N.R. and Prasad, B.V.S.S.S. Computational flow and heat transfer of a row of circular jets impinging on a concave surface. *Heat Mass Transf.* **2008**, 44, 667-678.
11. Choi, E.Y., Choi, Y.D., Lee, W.S., Chung, J.T. and Kwak, J.S. Heat transfer augmentation using a rib- dimple compound cooling technique. *Appl. Therm. Engg.* **2013**, 51(1-2), 435-441.
12. Singh, P. and Ekkad, S. Experimental study of heat transfer augmentation in a two-pass channel featuring 583 V-shaped ribs and cylindrical dimples. *Appl. Therm. Engg.* **2017**, 116, 205-216.
13. Gau, C. and Lee, I.C. Flow and impingement cooling heat transfer along triangular rib-roughened walls. 585 *Int. Heat Mass Transf.* **2000**, 43, 4405-4418.
14. Taslim, M.E., Setayeshgar and Spring, S.D. An Experimental Evaluation of Advanced Leading Edge Impingement Cooling Concepts. *ASME J. Turbomach.* **2001**, 123, 147-153.
15. Ekkad, S.V. and Kontrovitz, D. Jet impingement heat transfer on dimpled target surfaces. *Int. J. Heat Fluid 589 Flow* **2002**, 23, 22-28.
16. Xing, W. and Weigand, B. Experimental investigation of impingement heat transfer on a flat and dimpled 591 plate with different crossflow schemes. *Int. J. Heat Mass Transf.* **2010**, 53, 3874-3886.
17. Zhang, D., Qu, H., Lau, J. and Xie, Y. Flow and heat transfer characteristics of single jet impinging on protrusioned surface. *Int. J. Heat Mass Transf.* **2013**, 58, 18-28.
18. Jing, Q., Zhang, D. and Xie, Y. Numerical investigations of impingement cooling performance on flat and non-flat targets with dimple/protrusion and triangular rib. *Int. J. Heat Mass Transf.* **2018**, 126, 169-190.
19. Agarwal R.K., Bower, W.W. Navier-stokes computations of turbulent compressible two-dimensional 597 impinging jet flow fields. *AIAA J.* **1982**, 20(5), 577-584.
20. Ramezanpour, A., Shirvani, H., Mirzaee, I. A numerical study on the heat transfer characteristics of two-dimensional inclined impinging jet. *IEEE Electronics Packaging Tech. Conf.* **2003**, 626-632.
21. Rady, M., Arquies, E. Heat transfer enhancement of multiple impinging slot jets with symmetric exhaust parts and confinement surface protrusions. *Appl. Therm. Engg.* **2006**, 26(11-12), 1310-1319.
22. Sharif, M.A.R. and Mothe, K.K. Parametric study of turbulent slot-jet impingement heat transfer from concave cylindrical surfaces. *Int. J. Therm. Sci.* **2010**, 49, 428-442.
23. Kadam, A.R., Parida, R.K., Hindasageri, V., Kumar, G.N. Heat transfer distribution of premixed methane-air laminar flame jets impinging on ribbed surfaces. *Appl. Therm. Engg.* **2019**, 163, 114352-12.
24. Gau, C., Lee, C.C. Impingement cooling flow structure and heat transfer along rib-roughened walls. *Int. J. 607 Heat Mass Transf.* **1992**, 35, 3009-3020.
25. Labbé, O. Large-eddy-simulation of flow and heat transfer in a ribbed ducts. *Comput. Fluids* **2013**, 76, 23-32.

26. Haasenritter, A., Weigand, B. Optimization of the rib structure inside cooling channel with geneticalgorithms. *Int. J. Design Nature* **2007**, 1(2), 116-134.
27. Yang, Y.T., Chen, P.J. Numerical optimization of turbulent flow and heat transfer characteristics in a ribbed channel. *Heat Transf. Engg.* **2015**, 36, 290-302.
28. Damavandi, M.D., Safikhani, H., Yahyaabadi, M. Multi-objective optimization of asymmetric v-shaped ribs in a cooling channel using CFD, artificial neural networks and genetic algorithms. *J. Brazilian Society Mech. Sci. Engg.* **2017**, 39(6), 2319-2329.
29. Xi, L., Gao, J., Xu, L., Zhao, Z. Study on heat transfer performance of steam-cooled ribbed channel using neural networks and genetic algorithms. *Int. J. Heat Mass Transf.* **2018**, 127(C), 1110-1123.
30. Damavandi, M.D., Forouzanmehr M., Safikhani, H. Modeling and pareto based multi-objective optimization of wavy fin-and-elliptical tube heat exchangers using CFD and NSGA-II algorithm. *Appl. Therm. Engg.* **2017**, 111, 325-339.